



Low-temperature impedance spectroscopic analyses of ceramic electrodes based on Mo and Co co-doped SnO₂

Diego H.O. Ferreira¹, Isabela C.F. Vaz¹, Rero M. Rubinger², Camila Buono³, Leandro S.R. Rocha⁴, Miguel A. Ponce³, Elson Longo⁴, Alexandre Z. Simões^{5,*}, Francisco Moura¹

¹Universidade Federal de Itajubá, Unifei-Campus Itabira, Rua Irmã Ivone Drumond, 200, Distrito Industrial II, CEP 35903-087, Itabira, Minas Gerais, Brasil

²Universidade Federal de Itajubá, Unifei-Campus Itajubá, Av. BPS, 1303, Bairro Pinheirinho, CEP: 37500-903 Itajubá, Minas Gerais, Brasil

³University of Mar del Plata (UNMdP), Institute of Materials Science and Technology (INTEMA), National Research Council (CONICET), Av. Juan B. Justo 4302, 7600 Mar del Plata, Argentina

⁴Federal University of São Carlos (UFSCar), São Carlos, SP, Brazil

⁵Sao Paulo State University (Unesp), School of Engineering, Guaratinguetá, Brazil

Received 18 February 2019; Received in revised form 25 July 2019; Accepted 3 November 2019

Abstract

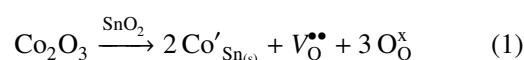
Low resistive electrodes based on Co and Mo co-doped SnO₂ were prepared by the conventional solid-state reaction and sintered at 1250 °C for 2 h. Concentration of Co₂O₃ precursor was unchanged (1 mol%), while MoO₃ was varied (0.25, 0.50 to 0.75 mol%) to promote conductivity. The structural and microstructural characterization revealed that the samples have a rutile-type structure without secondary phases and large rutile grains with low porosity. Electrical measurements on DC mode have shown a semiconductor behaviour of the SnO₂ samples doped with 0.25 and 0.75 at.% of Mo at temperatures below 50 K, indicating their suitability for low-temperature electronic applications. Impedance measurements indicate reduced energy barriers of less than 1 meV formed between highly conductive crystallites for the SnO₂ samples doped with 0.25 and 0.75 at.% of Mo. The sample with Mo content of 0.50 at.% presented a higher energy barrier at a few hundredths of eV, with space charges at the crystallite boundaries.

Keywords: Co/Mo co-doped SnO₂, complex impedance spectroscopy, low-temperature electronic applications

I. Introduction

Tin dioxide (SnO₂) is an n-type semiconductor with a rutile-type crystalline structure which has low densification rate due to its high surface tension at low temperatures and high SnO₂ partial pressure at high temperatures [1]. Dense SnO₂-based ceramics can be achieved by introducing dopants as well as by the hot isostatic pressing route [2]. The addition of cobalt(III) oxide (Co₂O₃) creates oxygen vacancies along with substituted cobalt atoms, expressed according to the Kröger-Vink notation as V_O^{••}, Co'_{Sn} or Co''_{Sn}, respec-

tively, which can segregate at the grain boundaries and assist in the formation of the Schottky barriers [3]. SnO₂ with tetragonal phase do not densify during the sintering process when the conventional solid-state method is employed, although dense SnO₂ ceramics are suitable for applications such as varistors [4], photochemical devices [5], electrodes for electric glass melting furnaces, and applications that request high chemical corrosion resistance [6]. In this way, Co₂O₃ is used to assist the densification process [6], ascribed to the replacement of Sn⁴⁺ by Co³⁺ species and the consequent creation of oxygen vacancies [7–9], likely facilitating the diffusion processes, according to the following reaction [10]:



*Corresponding author: tel: +55 12 3123 2228, e-mail: alezipo@yahoo.com

SnO₂ alloying can be engineered by controlling intrinsic and extrinsic defects. According to literature [11–13], intrinsic defects are presented mainly as oxygen vacancies and interstices while extrinsic defects can be added in order to act as donors or acceptors to the SnO₂ energy gap. The polycrystalline SnO₂ presents a band-tail-like energy gap close to the conduction band due to the doubly-ionized oxygen vacancies ($V_O^{\bullet\bullet}$) and by interstitial Sn ($Sn_i^{\bullet\bullet\bullet}$) acting as donors. When it comes to the sintering of polycrystalline ceramics, the high temperatures lead to the movement of ionic charges to the surface of crystallites with the consequent formation of potential barriers among them [18]. If the alloying level is sufficiently high, free carriers in the crystallites will recombine with space charges, lowering the potential barriers and allowing the metallic character of the conduction to occur. Increased electron density allows a reduction of the energy barriers which in turn affects the sample resistivity [16]. The potential barriers between crystallites act as an energy barrier that limits the charge transport, defining the resistivity as a function of the applied voltage (V_s), the electron charge (e) and effective mass (m^*), the Boltzmann constant (k_B), the sample temperature (T), the average crystallite size (L) determined from the Debye-Scherrer formula, and the free charge density (n). In the case of non-overlapped potential barriers, the energy barrier height (ϕ) can be assumed as equal to $e \cdot V_s$, shown in Fig. 1, which is defined as $(L^2 \cdot e^2 \cdot N_d)/(8 \cdot \epsilon \cdot \epsilon_0)$.

The $e \cdot V_s$ value can be determined by plotting $\ln(\rho T^{-1/2})$ versus $1000/T$. The applicability of this mo-

del is tested by the Debye-length (L_D) rule, i.e. if $L_D < L/2$, then the activation energy is due to carrier trapping by ionized deep-level defects at the crystallite boundaries [19]. L_D can be defined as $[(k_B \cdot T \cdot \epsilon \cdot \epsilon_0)/e^2 \cdot N_d]^{1/2}$, where ϵ is the low frequency dielectric permittivity determined by the impedance spectroscopy measurements [20], also carried out in this work, and ϵ_0 the vacuum permittivity. Figure 1 shows an energy band diagram representation of the mentioned parameters. Our samples correspond to the case shown in Fig. 1a where potential barriers are not overlapped as a consequence of an $L_D < L/2$. In this case, the barrier height ϕ can be assumed as equal to the band bending $e \cdot V_s$.

Therefore, distinct proportions of molybdenum oxide (MoO₃) were used as extrinsic donors since molybdenum (Mo) presents 6 electrons in the outer orbitals, in order to investigate its influence on the SnO₂ conductivity [14,15]. It is an attempt to open perspectives for application of Mo and Co co-doped SnO₂ towards low-temperature applications in aerospace and information transmission lines semiconductors. We also have to consider that the Mo-doping into the SnO₂ lattice induces the formation of Sn_(s) vacancies [10]. In this way, the low-temperature impedance spectroscopy (IS) technique has also been used to study the influence of the MoO₃ addition on the three main contributions of the electrical conductivity in a polycrystalline solid: bulk and internal surfaces like grain boundaries and electrodes [17]. Often, for a better analysis of the impedance measurements, the imaginary (complex) and the real components are plotted as a Nyquist diagram. This is accomplished by varying the frequency of the AC input signal over a wide range in order to cover the different responses that charge carriers show inside grains, at grain boundaries and at the specimen-electrode interface. In this work, we propose a complementary study in which the total parallel equivalent capacitance (C_p) and the total parallel resistance (R_p) as a function of frequency are also analysed in order to calculate different currents contributions in this type of semiconductor. On this way, we might be able to estimate barriers height and width, as well as their donor concentration for different samples.

II. Materials and methods

The powders were prepared using analytical grade tin oxide (SnO₂, 99.9%), cobalt(III) oxide (Co₂O₃, 99.99%), and molybdenum oxide (MoO₃, 99.50%). The conventional mixed oxide method was performed in a Marconi MA 500/CF ball mill, during 24 h at 150 rpm, using isopropyl alcohol (200 ml/10 mg of powder) and yttria-stabilized zirconia (YSZ) balls. After milling, the samples were dried in a SP Labor SP-400 laboratory oven at 100 °C for 12 h. The powders were then uniaxially pressed with 11 MPa in steel moulds with a diameter of 8.5 mm and then isostatically pressed at 200 MPa during 60 s in ethyl alcohol, using a Mar-

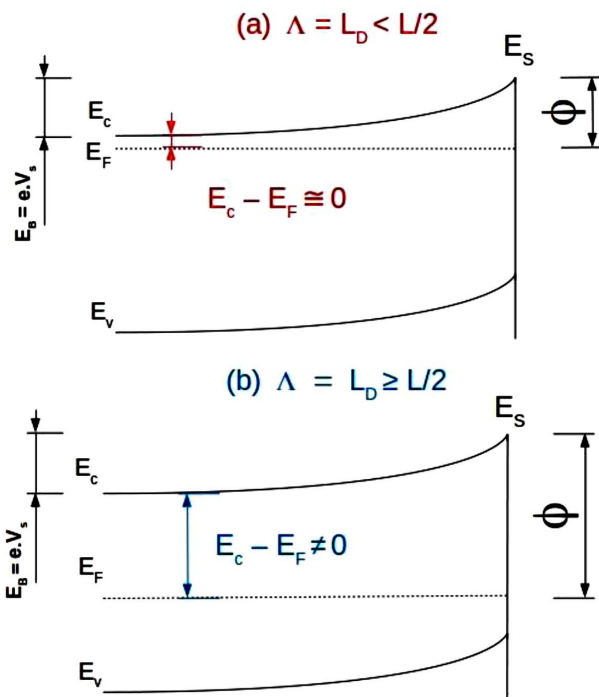


Figure 1. Schematic of Debye-length rule representing the non-overlapped (a) and overlapped potential barriers (b)

con MPH-30 isostatic press. To promote densification of the SnO_2 , concentration of cobalt(III) oxide precursor was unchanged (1 mol%), while MoO_3 was varied from 0.25 to 0.75 mol% to promote conductivity. The molar compositions of the investigated systems were $(99-x)\text{SnO}_2 + 1\text{Co}_2\text{O}_3 + x\text{MoO}_3$, with $x = 0.25, 0.50$ and 0.75 mol%. The samples were named A1, A2 and A3 with the following conditions: A1 ($x = 0.25$), A2 ($x = 0.50$) and A3 ($x = 0.75$). The sintering process occurred at 1250 °C in a muffle oven with air atmosphere, and a heating rate of 5 °C/min for 2 h.

In order to determine the crystalline phase, structural characterizations by X-ray diffraction (XRD) were made in a Rigaku DMax/2500PC with an acceleration voltage of 40 kV and a current of 15 mA using $\text{Cu-K}\alpha$ radiation ($\lambda = 1.5418740 \text{ \AA}$). The measured angular range (2θ) was 20° to 75° with a step of 0.05°. The scanning electron microscopy (SEM) investigations were carried out using a Tescan See 3SEM, with an acceleration voltage of 3 kV, aiming to determine the average crystallite sizes as well as the mean grain sizes. The DC and AC electrical measurements were applied in order to determine the dielectric and conductive properties in a Janis CCS-350T closed cycle cryostat (from 10 to 317 K), with a Keithley 2400 source/measure unit along

with a Novocontrol Alpha-A impedance analyser, with the frequency ranging from 0.01 Hz to 10 MHz in air (~20% oxygen) [18,19]. The electrical resistance and capacitance were determined and fitted with an R(RC) equivalent circuit using the software Zview 2.1. A sequential number of measurements was carried out for each sample. Density measurements were made using the Archimedes method.

III. Results and discussion

3.1. Crystallographic characterization

Figure 2 shows the X-ray diffraction patterns of the sintered Co and Mo co-doped SnO_2 pellets. Besides the SnO_2 rutile-like character, no secondary phase due to the Co_2O_3 and MoO_3 addition was noted. A sintering study combined with the XRD results indicated that the temperature of 1250 °C for 2 h is the optimal to obtain crystalline and dense Co and Mo co-doped SnO_2 containing only the expected rutile phase. All dopants introduced in the SnO_2 matrix lead to a stable solid solution according to the Eqs. 1 and 2.

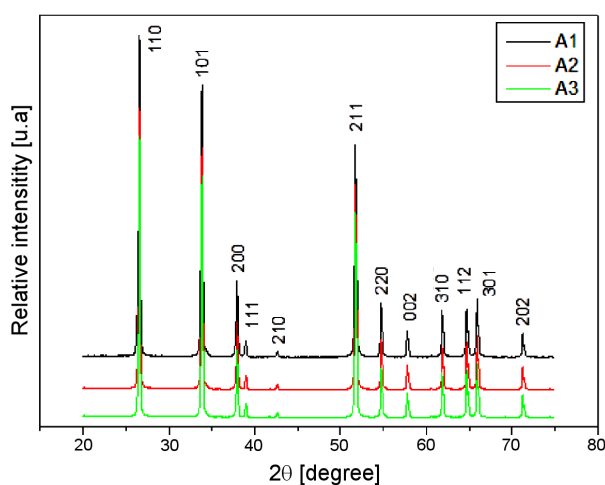
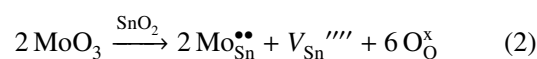


Figure 2. X-ray diffraction data of the ceramic pellet samples with different Mo content: A1, A2 and A3

3.2. Microstructural characterization

Figure 3 shows the SEM micrographs of the doped SnO_2 samples sintered at 1250 °C and physical dimensions and microstructural characteristics of the conformed varistors are given in Table 1. Considering their microstructure, a Schottky-type electrical barrier can be likely considered at the SnO_2 grain boundaries, since no intergranular insulating layers in between grains were observed. The negative surface charge at the

Table 1. Physical dimensions and microstructural characteristics of the conformed varistors

	A1	A2	A3
Area, S [$\text{m}^2 \times 10^{-5}$]		5.67	
Block thickness, d [mm]		1	
Grain size [μm]	3.02	8.04	4.65
No. of grains in thickness, d	331	124	215

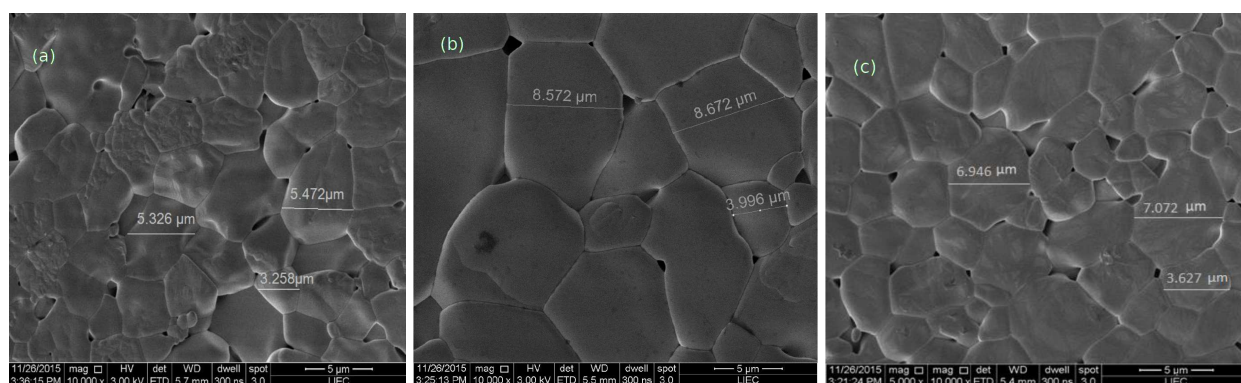


Figure 3. SEM micrographs for the ceramic electrode system with different Mo content: a) 0.25 (A1), b) 0.50 (A2) and c) 0.75 at.% (A3)

grain boundary interface is compensated by the positive charge in the depletion layer in the grains on both sides of the interface [20–22]. SEM images confirm low pore density between adjacent grains. The addition of molybdenum does not provided a linear reduction in grain size, as we can see from Fig. 3. After sintering, the sample A1 (Fig. 3a) has an increase of the density from 56.12 ± 1.04 to $92.3 \pm 1.4\%$ TD, with an average grain size of $3.02 \mu\text{m}$ determined by the linear intercept method. While the density of the samples A2 and A3 increased from 58.57 ± 1.67 to $89.53 \pm 0.30\%$ TD and from 58.28 ± 1.55 to $92.37 \pm 1.24\%$ TD, respectively. A low pore density between grains can also be seen, without formation of secondary phases. The SnO_2 ceramics densification has been mainly attributed to the effect of dopants substitution in the SnO_2 matrix which leads to the formation of oxygen vacancies, providing the increase of the diffusion coefficient of ions, and thus, promoting the sintering. Cerri *et al.* [3] found relative density above 99% TD, showing that CoO is extremely active in the promotion of the SnO_2 densification, even

with low concentration of dopants. They attributed the high densification to the increased concentration of oxygen vacancies in the grain boundary region, with the proposed reaction for the formation of oxygen vacancies when SnO_2 is doped with Co. These results are in agreement with the work of Yuan *et al.* [23] who demonstrated that the Li^+ ion also promotes SnO_2 densification by increasing the flux of species that diffuse inside the material. Pianaro *et al.* [24] observed that when the basic SnO_2 varistor is doped with Cr_2O_3 the grain size decreased, indicating that Cr_2O_3 inhibits grain growth during sintering.

3.3. Impedance spectroscopy

Figure 4a presents the impedance arcs (Nyquist plots) for the samples A1, A2 and A3 in the frequency range of 0.01 Hz to 10 MHz, at 300 K. An inset is used to evidence the arcs of the samples A1 and A3 that presented a much lower impedance when compared to the sample A2. The observed behaviours of the varistors cannot be reproduced with simple RC circuits (Fig. 4a, A2-

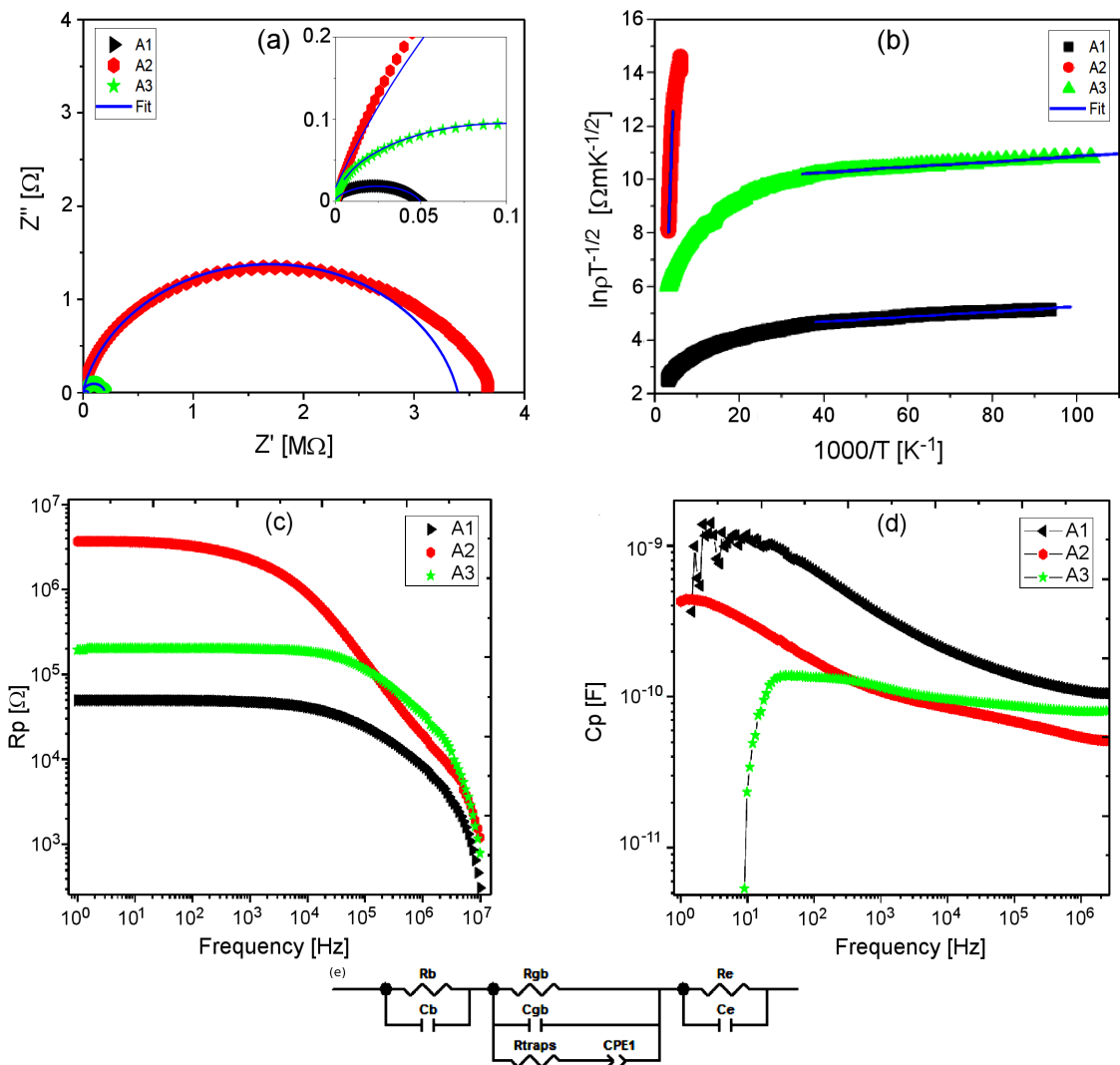


Figure 4. Complex impedance spectroscopy for samples A1, A2 and A3 in the form of: a) Nyquist plot, b) resistivity versus $1000/T$, c) R_p versus frequency, d) C_p versus frequency, along with e) equivalent electric circuit

Table 2. Density currents, barrier heights, barrier widths, donor concentrations, as well as the electrical parallel capacitance (C_p) and resistance (R_p) from the experimental measurements

Sample	$e \cdot V_s$ [eV]	ϕ [eV]	Λ [nm]	N_d [10^{24} m^{-3}]	J [$\text{A}/\text{m}^2 \times 10^{-5}$]	C_p (at 1 MHz) [pF]	R_p (at 10 Hz) [k Ω]
A1	0.999	1.001	19.40	3.31	3.6559	109	48.0
A2	0.074	1.026	26.68	1.26	0.0046	51.5	3890
A3	0.082	1.018	23.72	1.71	0.1444	80.65	121

fitting), which indicates that a more refined electrical circuit model must be considered [25]. The resistivity data up to 300 K in a $\ln(\rho T^{-1/2})$ versus $1000/T$ plot can be seen in Fig. 4b. In this plot, a linear slope indicates that barriers at the crystallite boundaries are present and that this model is applicable. Fittings for a standard parallel circuit model are represented in Table 2 along with permittivity data. In Figs. 4c and 4d, the electrical parallel capacitance and resistance of the samples are plotted as a function of frequency at a fixed temperature of 300 K. An increase in C_p , Fig. 4c, at low frequencies corroborates the presence of deep bulk traps. Moreover, Fig. 4d shows that grain size differences could not be responsible for the change in resistance. Furthermore, it can also be a consequence of narrow inter-granular barriers formation that facilitates conduction. In the circuit in Fig. 4e, three different contributions to the overall impedance were postulated: grain boundary, bulk traps and electrode contact. The electrical behaviour of a varistor at low frequencies can be described with the electrical model shown in Fig. 4e. In this circuit, the resistance R_{traps} and the CPE mimics the effect of deep traps [26]. In Figs. 4c and d, it can be observed that grain size differences (Table 1) are not directly correlated with changes of C_p (at 1 MHz) and R_p (at 10 Hz) for the samples A1, A2 and A3. Figure 4c also indicates mild capacitance dependence with the frequency for the samples at 1 MHz. Conversely, for the samples A1 and A2, a significant increase of the slope (C_p vs. bias) from 1000 to 1 Hz is observed. This dependence is another evidence of the grain boundary barriers and traps phenomenon in these grains. The sample A3 presents an inductive behaviour at low frequencies. This phenomenon could be associated with the MoO_3 addition. For no bias, the grain boundary capacitance measurements are shown in Table 2.

Using the parameters given in Table 1, we study the electrical conductance and capacitance variations with Mo-doping. This information allows us to estimate band bending ($e \cdot V_s$), the barrier height (ϕ), the width (Λ or L_D) and the donor concentration (N_d), depicted in Table 2. Therefore, it is necessary to consider the two main electrical mechanisms contributions of tunnelling and thermionic currents to the total conductivity. Then we can model the electrical behaviour using an equivalent electronic circuit to obtain the relevant electrical components (grain boundary capacitance and grain boundary resistance) which permit to obtain the fitting values for total current components (tunnel and thermionic).

For the samples used in the present work one could

assume that at the interface of the grains, the pellets present non-overlapped Schottky-type potential barriers with ($\Lambda < L/2$) due to the grain sizes (Table 1). Then, the electrical behaviour of the metal oxide pellets could be regularly modelled using an (RC) electrical equivalent circuit. However, in previous works, we have shown that this simple circuit did not suffice to reproduce the impedance frequency responses and that a more sophisticated model needed to be considered [27]. Such a model, including electrode and bulk effects, deep bulk traps, and grain boundaries is shown in Fig. 4e. In order to simplify the model, we have assumed that R_b can be neglected at low frequencies [27]. In this circuit, the resistance R_t and the capacitance C_t mimic the effect of deep traps [26]. The total conductivity (G_p) and total capacitance (C_p) for this type of circuits can be expressed as:

$$G_p = \frac{1}{R_{gb}} + C_t \cdot \omega^2 \frac{\tau}{1 + \omega^2 \cdot \tau^2} \quad (3)$$

and

$$C_p = C_{gb} + C_t \frac{\tau}{1 + \omega^2 \cdot \tau^2} \quad (4)$$

where $\tau = C_t \cdot R_t$ is the traps' mean lifetime. R_{gb} and C_{gb} values, defined by Eqs. 3 and 4, can be determined by taking the limit values of the conductance and capacitance for very low and very high frequencies as:

$$G_{tot, \omega \rightarrow 0} = \frac{1}{R_{gr}} \quad (5)$$

and

$$G_{p, \omega \rightarrow 0} = C_{gb} \quad (6)$$

In order to study grain boundary capacitance changes, we can consider the C_{gb} at a frequency of 1 MHz ($C_p \approx C_{gb}$). Also, for our working frequency, the electrode effects on total impedance and total capacitance can be estimated assuming a quite high value for the electrode capacitance (10^{-5} F) [28].

Figure 5 shows the electrical capacitance behaviour of the possible grain boundary barriers analysed at 1 MHz for a bias of 0 V. The total capacitance dependence on frequency is affected by the presence of deep bulk traps. These bulk traps have a distribution of activation energies that implies a distributed impedance element. A simple distributed phase element, called constant phase element (CPE), has a constant phase angle in the complex plane and reflects the microscopic material inhomogeneities [29].

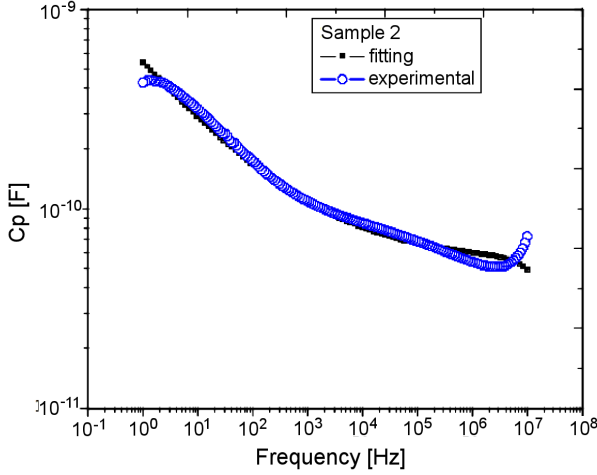


Figure 5. Parallel capacitance (C_p) versus frequency (f) along with a curve fitting for the sample A2

With the information given in Table 1 we have calculated the capacitance considering that we are dealing with a homogeneous material. For potential barriers, the capacitance of an inter-grain is that of two Schottky barriers in series. This change can be interpreted as a consequence of depletion widths that are narrower than the grain radius (non-overlapped potentials barriers), due to a higher doping. The band bending ($e \cdot V_s$) and width (Λ) in a Schottky barrier can be directly related using [30]:

$$e \cdot V_s = \frac{e \cdot N_d}{2\epsilon} \Lambda^2 \quad (7)$$

where N_d is the donor concentration. N_d can be estimated considering a typical value of barrier height of 1 eV (value that we will confirm below) using the relation of Eq. 7:

$$N_d = \frac{2\epsilon \cdot e \cdot V_s}{2\epsilon} \Lambda^2 \quad (8)$$

The dopant concentration can also be determined considering the capacitance for n intergrains in series:

$$\frac{1}{C_{gb}} = 2 \left(\frac{2e \cdot V_s \cdot n^2}{e \cdot \epsilon \cdot N_d \cdot S^2} \right)^{1/2} \quad (9)$$

where $e \cdot V_s$ is given in Volts. Equation 9 corresponds to the capacitance obtained from measurements shown in Fig. 5. N_d can be calculated from C_{gb} as:

$$N_d = C_{gb}^2 \cdot e \cdot V_s \frac{8n^2}{q \cdot \epsilon_r \cdot \epsilon_0 \cdot S^2} \quad (10)$$

With Eq. 10, the value for the dopant concentration can be determined, $N_d \sim 10^{24} \text{ m}^{-3}$, which is quite close to the one determined using Eq. 8.

To gain confidence in the previous analysis based on capacitance measurements, we have calculated theoretically the total current due to both tunnelling and thermionic emission in order to fit the experimental values.

On one hand, the total current density over and through a barrier can be calculated as [30]:

$$J = \frac{A \cdot T}{k} \int_0^{e \cdot V_s} f(E) P(E) dE + A \cdot T^2 \exp\left(-\frac{e \cdot f}{k_B \cdot T}\right) \quad (11)$$

The first term of Eq. 11 corresponds to the tunnelling current while the second term is the thermionic contribution to the total current, A and k_B are the Richardson and Boltzmann constants respectively, and $f(E)$ is the Fermi-Dirac distribution. $P(E)$, the transmission probability for a reverse-biased Schottky barrier, which is the limiting step, as previously explained [31–34] is given by:

$$P(E) = \exp\left[-\frac{4\pi e V_s}{qh} \left(\frac{m\epsilon}{N_d}\right)^{1/2} \ln\left(1 - \left(1 - \frac{E}{eV_s}\right)^{1/2}\right)\right] \quad (12)$$

where m is the electron effective mass, ϵ the electrical permittivity ($\epsilon_r = 14$ for SnO_2) and h is the Planck constant.

On the other hand, the experimental current density (J_{exp}) can be obtained from the grain boundary resistance (Fig. 3d) with the following relationship:

$$J_{exp} = \frac{V}{S} R_{gb(20 \text{ Hz})} \quad (13)$$

where V is the applied voltage during impedance spectroscopy measurements, S the varistor area ($6.5 \times 10^{-5} \text{ m}^2$) and R_{gb} the grain boundary resistance measured at low frequencies. Then, pairs of N_d and $e \cdot V_s$ were used for fitting experimental values with Eqs. 3–13. Iterative numerical calculations were carried out until the calculated total current density J from Eq. 11 was equal to the experimental value J_{exp} obtained with Eq. 13. Results of N_d and $e \cdot V_s$ are shown in Table 2 confirming our previous estimations. In this way the fittings for the sample A2 were carried out. The capacitance plot was fitted as a function of frequency at 300 K in air atmosphere considering the electrical equivalent circuit proposed in Fig. 4e. The employed element values are shown in Table 3. The electrical behaviour of tin oxide varistor was modelled using a (RC) parallel equivalent circuit, using a refined model. The AC resistance and capacitance measurements at low frequencies indicate deep bulk traps presence at SnO_2 samples. Also, by using the equivalent circuit from Fig. 4e, and considering the tunnelling conduction contribution, we can understand the influence of donor concentrations on the resistance and capacitance. Finally, it is important to mention that C_p (at 1 MHz) and R_p (at 10 Hz) changes for the samples A1, A2 and A3 were not directly correlated with grain size differences (see Table 1) as shown in Eqs. 9 and 10. Instead, the main changes for C_p (at 1 MHz) and R_p (at 10 Hz) are attributed to the barrier height ($\phi = e \cdot V_s$) and width (Λ) values independently of grain size.

Table 3. Employed element values for the proper fitting of C_p versus frequency for sample A2

Circuit element	Values
Bulk Resistance, R_b [Ω]	100
Bulk Capacitance, C_p [F]	10^{-12}
Grain boundary resistance, R_{gb} [Ω]	3.7×10^6
Grain boundary capacitance, C_{gb} [F]	5.5×10^{-11}
Electrode resistance, R_e [Ω]	10
Electrode capacitance, C_e [F]	10^{-5}
Deep bulk traps resistance, R_t [Ω]	10^3
Deep bulk traps capacitance [F]	10^{-9}
CPE α coefficient	0.68

IV. Conclusions

Low resistive electrodes based on Co and Mo co-doped SnO₂ were prepared by the conventional solid-state reaction and sintered at 1250 °C for 2 h. Their morphological and structural properties were investigated by SEM and XRD indicating the presence of large rutile grains with low porosity. These materials are presented in the form of inter and intra clusters of crystallites of about 3 μ m. The addition of molybdenum did not provide a linear shift in average grain sizes, though a higher densification was obtained, likely ascribed to the increased concentration of oxygen vacancies after modification with Co₂O₃ that diffused towards the surface facilitating the sintering process. This high density of ionized impurities, according to electrical measurements, have migrated to crystallite boundaries and built up a potential barrier that limited charge transport even at room temperature. For this reason, only the samples with 0.25 at.% and 0.75 at.% of Mo content would be suitable for use as electrodes for low-temperature operations. Deep bulk traps in SnO₂ ceramics co-doped with Co and Mo were evidenced using AC resistance and capacitance measurements.

The co-doped SnO₂ ceramics presented an independence from grain size variation in the electrical resistance control, with the inter-granular potential barrier height (ϕ) having a key dependence on doping effects, which reflects on non-overlapped potential barriers where the Fermi level energy (E_F) is close to the conduction band (E_C), and therefore $\phi = e \cdot V_s$.

Acknowledgement: The authors gratefully acknowledge the financial support of the agencies FAPEMIG APQ-03589-16, CNPq 573636/2008-7, INCTMN 2008/57872-1, FAPESP 2013/07296-2, FAPESP 2018/07238-6, FAPESP 2018/20590-0, and CAPES.

References

- J.G. Fagan, R.W. Amarakoon, "Reliability and reproducibility of ceramic sensors", *Am. Ceram. Soc. Bull.*, **72** (1993) 119–130.
- S.J. Park, K. Hitota, H. Yamamura, "Densification of non-additive SnO₂ by hot isostatic pressing", *Ceram. Int.*, **10** (1984) 115–116.
- J.A. Cerri, E.R. Leite, D. Gouvea, E. Longo, J.A. Varela, "Effect of cobalt(II) and manganese(IV) on sintering of tin(IV) oxide", *J. Am. Ceram. Soc.*, **79** (1996) 799–804.
- S.A. Pianaro, P.R. Bueno, P. Olivi, E. Longo, J.A. Varela, "Effect of Bi₂O₃ addition on the microstructure and electrical properties of the SnO₂·CoO·Nb₂O₅ varistor system", *J. Mater. Sci. Lett.*, **16** (1997) 634–638.
- Z.M. Jarzebski, J.P. Marton, "Physical properties of SnO₂ materials: II. Electrical properties", *J. Electrochem. Soc.*, **123** [9] (1976) 299C–310C.
- M. Zaharescu, S. Mihaeu, S. Zuca, K. Matiasovsky, "Contribution to the study of SnO₂-based ceramics", *J. Mater. Sci.*, **26** (1991) 1666–1672.
- J.A. Varela, D. Gouvea, E. Longo, N. Dolet, M. Onillon, J.P. Bonnet, "The effect of additives on the sintering of tin oxide", *Solid State Phenom.*, **25** (1992) 259–268.
- J.A. Varela, O.J. Whittemore, E. Longo, "Pore size evolution during sintering of ceramic oxides", *Ceram. Int.*, **16** (1990) 177–189.
- C.R. Foschini, L. Perazolli, J.A. Varela, "Sintering of tin oxide using zinc oxide as a densification aid", *J. Mater. Sci.*, **39** (2004) 5825–5830.
- P.R. Bueno, S.A. Pianaro, E.C. Pereira, E. Longo, J.A. Varela, "Investigation of the electrical properties of varistor system using impedance spectroscopy", *J. Appl. Phys.*, **84** (1998) 3700–3705.
- J.A. Varela, J.A. Cerri, E.R. Leite, E. Longo, M. Shamsuz-zoha, R.C. Bradt, "Microstructural evolution during sintering of CoO doped SnO₂ ceramics", *Ceram. Inter.*, **25** (1999) 253–256.
- A.L. Perazolli, C.R. Foschini, T.R. Giraldo, R.S. Biscaro, J.A. Varela, E. Longo, "Improved densification of SnO₂ by doping with ZnO", *Sintering Sci. Technol.*, **23** (2000) 117–122.
- F.A. Kröger, H.J. Vink, "Relations between the concentrations of imperfections in crystalline solids", *Solid State Physics*, **3** (1956) 307–465.
- H.S. Irion, "Cerâmica varistora à base de SnO₂ dopado com Pr₆O₁₁", *M.Sc. thesis*, Universidade Estadual de Ponta Grossa, Ponta Grossa, Brazil, 2006.
- D.R. Leite, M. Cilense, M. Orlandi, P.R. Bueno, E. Longo, J.A. Varela, "The effect of TiO₂ on the microstructural and electrical properties of low voltage varistor based on (Sn,Ti)O₂ ceramics", *Phys. Stat. Solid A: Appl. Mat. Sci.*, **207** (2010) 457–461.
- S. Mohammadi, H. Abdizadeh, M.R. Golobostanfard, "Opto-electronic properties of molybdenum doped indium tin oxide nanostructured thin films prepared via sol-gel spin coating", *Ceram. Int.*, **39** (2013) 6953–6961.
- B.A. Boukamp, "A nonlinear least squares fit procedure for analysis of immittance data of electrochemical systems", *Solid State Ionics*, **20** (1986) 31–44.
- S. Saukko, V. Lantto, "Influence of electrode material on properties of SnO₂-based gas sensor", *Thin Solid Films*, **436** (2003) 137–140.
- K.S. Cole, R.H. Cole, "Dispersion and absorption in dielectric I. Altering current characterizations", *J. Chem. Phys.*, **9** (1941) 341–351.
- P.R. Bueno, M.R. Cassia-Santos, E. Longo, "Nature of the Schottky-type barrier of highly dense SnO₂ systems displaying nonohmic behavior", *J. Appl. Phys.*, **88** (2000) 6545–6550.
- D.M. Radecka, K. Zakrezewska, M. Rekas, "SnO₂-TiO₂ solid solutions for gas sensors", *Sensors Actuators B:*

- Chem.*, **47** (1998) 194–198.
22. T.K. Gupta, “Application of zinc oxide varistors”, *J. Am. Ceram. Soc.*, **73** (1990) 1817–1840.
 23. D. Yuan, S. Wang, W. Huebner, G. Simkovich, “The effect of Li-salt additions on the densification of tin oxide”, *J. Mater. Res.*, **8** [7] (1993) 1675–1679.
 24. S.A. Pianaro, P.R. Bueno, P. Olivi, E. Longo, J.A. Varela, “Electrical properties of the SnO₂ based varistor”, *J. Mater. Sci.: Mater. Electron.*, **9** (1998) 159–164.
 25. F. Schipani, D.R. Miller, M.A. Ponce, P. Morris, “Electrical characterization of semiconductor oxide-based gas sensors using impedance spectroscopy: A review”, *Rev. Adv. Sci. Eng.*, **5** (2016) 86–105.
 26. B.S. Chiou, M.C. Chung, “Admittance spectroscopy and trapping phenomena of ZnO based varistors”, *J. Electron. Mater.*, **20** (1991) 885–889.
 27. M.A. Ponce, M.S. Castro, C.M. Aldao, “Capacitance and resistance measurements of SnO₂ thick-films”, *J. Mater. Sci.: Mater. Electron.*, **20** (2009) 25–32.
 28. A.K. Jonscher, J.M. Réau, “Analysis of the complex impedance data for β -PbF₂”, *J. Mater. Sci.*, **13** (1978) 563–570.
 29. T.P. Hulser, H. Wiggers, F.E. Kruis, A. Lorke, “Nanostructured gas sensors and electrical characterization of deposited SnO₂ nanoparticles in ambient gas atmosphere”, *Sensors Actuators B: Chem.*, **109** (2005) 13–18.
 30. R. Parra, M.A. Ponce, C.M. Aldao, M.S. Castro, “Advances in the study of the conduction modes in SnO₂ varistors”, *J. Eur. Ceram. Soc.*, **27** (2007) 3907–3909.
 31. M.S. Castro, C.M. Aldao, “Prebreakdown conduction in zinc oxide varistors: Thermionic or tunnel currents and one-step or two-step conduction processes”, *Appl. Phys. Lett.*, **63** (1993) 1077–1079.
 32. M.S. Castro, C.M. Aldao, “Thermionic, tunnelling, and polarization currents in zinc oxide varistors”, *J. Eur. Ceram. Soc.*, **17** (1997) 1533–1537.
 33. J. Robertson, “Defect levels of SnO₂”, *Phys. Rev. B*, **30** (1984) 3520–3522.
 34. M.P. Groover, *Fundamentals of Modern Manufacturing: Materials, Processes and Systems*, McGraw Hill, 1997.